Article

Heat Transport Exploration for Hybrid Nanoparticle (Cu, Fe₃O₄)—Based Blood Flow via Tapered Complex Wavy Curved Channel with Slip Features

A. Abbasi [1], W. Farooq [1], El Sayed Mohamed Tag-ElDin [2], Sami Ullah Khan [3], M. Ijaz Khan [4,5,*], Kamel Guedri [6,7], Samia Elattar [8], M. Waqas [9,*] and Ahmed M. Galal [10,11]

1. Department of Mathematics, University of Azad Jammu and Kashmir Muzaffarabad, Muzaffarabad 13100, Pakistan
2. Faculty of Engineering and Technology, Future University in Egypt, New Cairo 11835, Egypt
3. Department of Mathematics, COMSATS University Islamabad, Sahiwal 57000, Pakistan
4. Department of Mathematics and Statistics, Riphah International University I-14, Islamabad 44000, Pakistan
5. Department of Mechanical Engineering, Lebanese American University, Beirut 2100, Lebanon
6. Mechanical Engineering Department, College of Engineering and Islamic Architecture, Umm Al-Qura University, P.O. Box 5555, Makkah 21955, Saudi Arabia
7. Research Unity: Materials, Energy and Renewable Energies, Faculty of Science of Gafsa, University of Gafsa, Gafsa 2100, Tunisia
8. Department of Industrial & Systems Engineering, College of Engineering, Princess Nourah bint Abdulrahman University, P.O. Box 84428, Riyadh 11671, Saudi Arabia
9. NUTECH School of Applied Sciences and Humanities, National University of Technology, Islamabad 44000, Pakistan
10. Mechanical Engineering Department, College of Engineering, Prince Sattam Bin Abdulaziz University, Wadi Addawaser 11991, Saudi Arabia
11. Production Engineering and Mechanical Design Department, Faculty of Engineering, Mansoura University, Mansoura 35516, Egypt
* Correspondence: mikhan@math.qau.edu.pk or ijazfmg_khan@yahoo.com (M.I.K.); mw_qau88@yahoo.com (M.W.)

Abstract: Curved veins and arteries make up the human cardiovascular system, and the peristalsis process underlies the blood flowing in these ducts. The blood flow in the presence of hybrid nanoparticles through a tapered complex wavy curved channel is numerically investigated. The behavior of the blood is characterized by the Casson fluid model while the physical properties of iron (Fe₃O₄) and copper (Cu) are used in the analysis. The fundamental laws of mass, momentum and energy give rise the system of nonlinear coupled partial differential equations which are normalized using the variables, and the resulting set of governing relations are simplified in view of a smaller Reynolds model approach. The numerical simulations are performed using the computational software Mathematica's built-in ND scheme. It is noted that the velocity of the blood is abated by the nanoparticles' concentration and assisted in the non-uniform channel core. Furthermore, the nanoparticles' volume fraction and the dimensionless curvature of the channel reduce the temperature profile.

Keywords: Casson hybrid nanoparticles; peristaltic transport; slip effects; hall applications; numerical approach

1. Introduction

In various thermal techniques, the improvement of heat transfer with the proper utilization of nanofluids has emerged as a superior mechanism. Despite the continuous work in nanotechnology and thermal engineering reporting different means of enhancing the thermal processes, the results of increasing thermal resources have been notably poor due to high casting and low thermal performance. The nanoparticles in question are small sized metallic materials with good thermal accuracy. Recently, nanofluids have been used

in different applications such as energy production, various engineering phenomena, as industrial resources, for thermal management, etc. In recent years, nanoparticles have been widely used in anti-cancer drugs to kill tumor cells and due to their enhanced thermal conductivity these nanoparticles destruct the tumor tissue more efficiently. In cancer treatment, nanoparticles are inserted into the bloodstream to increase therapeutic efficacy and reduce side effects; better performance can be obtained by inserting different combinations of nanoparticles. Compelling improvements in the thermal properties of nanofluids are a fundamental source of motivation. Choi [1] performed the directions first on nanofluids; Buongiorno [2] endorsed the Brownian motion and the role of thermophoretic forces on nanofluid flows; Sui et al. [3] observed heat transfer fluctuation for the slip flow of nanofluids with a rate-type Maxwell model; Sandeep and Animasaun [4] conducted research to highlight the change in thermal properties of nanofluid when variable sources of thermal properties are followed; and Afridi et al. [5] reflected the heat transfer onset of nanofluids in view of fractional heat sources. The convective thermal case associated with the couple stress nanofluid has been analytically reported in the contribution of Khan et al. [6]. Kumar et al. [7] reported the entropy generation involvement for the Joule heating flow in the presence of radiative phenomenon. Khan et al. [8] preserved the microorganisms' suspension in nanofluids and inspected the stability analysis. The variable viscosity utilization for observing the nanofluid properties was noted by Mondal and Pal [9]. Ahmad et al. [10] determined the bioconvection investigation in a porous medium with nanoparticles' attention. Makinde et al. [11] predicted the thermal investigation based on nanofluids with magneto-hemodynamic applications. Das et al. [12] focused on the fully developed vertically moving channel flow of nanofluids under the influence of wall surface conductivity. Mandal et al. [13] worked out a nanofluid model for carbon nanotubes comprising the rotating 3-D flow. Zhang et al. [14] discussed the bioconvective attribution of nanofluids in concentric cylinders with a dominant Lorentz force contribution. The Walter-B nanofluid flow with attention to buoyancy forces has been analyzed in the work of Chu et al. [15].

The hybrid nanofluid is a superior category of nanofluids which reflects the improved thermal consequences of the suspension of two different nanoparticles in a base material. The motivation to observe the thermal mechanism of the base fluid via the hybrid nanofluid is due to the enhanced thermal mechanism. The reflection of hybrid nanofluid models exhibit more fascinating behavior than nanofluids. Special applications of hybrid nanofluids are observed in energy production, manufacturing systems, solar applications, heating devices, engine heat rate countering, extrusion processes, etc. The class of hybrid nanofluids is achieved after combining the base material with more than one nanoparticle. The thermal onset of hybrid particles is more stable and impressive. Wahid et al. [16] observed the thermal attention of hybrid nanofluids to a moving disk with permeable surface walls. Almaneea et al. [17] focused on the comparative enhancement of the thermal aspect of the heating phenomenon in view of hybrid nanofluid interaction. Mousavi et al. [18] investigated the flow of a stretching porous space encountering the hybrid nanofluid model and detected some dual numerical solutions in a confined region. The thermal effects of a hybrid nanofluid under the impact of a magnetic force were visualized by Khan et al. [19]. Madhukesh et al. [20] determined the curved geometry flow due to the hybrid nanofluid by observing the Newtonian heating effects. Rashid et al. [21] analyzed the heating aspect of titanium oxide in a moving cylinder in the horizontal direction. Abdelmalek et al. [22] identified the rotation of the disk flow where the improvement in heat transfer was influenced by hybrid nanoparticles. Muhammad et al. [23] predicted the attention of hybrid nanofluid to the squeezing flow. Shaw et al. [24] reported the contribution of the quadratic radiative phenomenon while working on Casson hybrid nanoparticles for various values of the Prandtl number. Sen et al. [25] developed tiny hybrid nanoparticles of thermal significance with a diamond base material. Nayak et al. [26] observed a distinct nanostructure for non-Newtonian fluids. The enrollment of interesting Darcy–Forchheimer forces for optimized nanofluid flow was addressed by Nayak et al. [27]. Recently, the work of Shaw [28] presented the various novel consequences of a hybrid

nanofluid model for rotatory disk flow. Mahanthesh et al. [29] observed the importance of Joule heating for hybrid nanofluid transport in a wedge capturing the isothermal properties. The permeable surface flow of hybrid nanofluid with theoretical observations has been determined by Haq et al. [30].

The application of the Hall effect is associated with direct current and is important in plasma physics, magnetic devices, electromagnetic theory, semi-conductors, voltage currents, circuit problems and various electrically conducting flows. The Hall current attains direct association with the magnetic force. Seth et al. [31] addressed the Hall effect for rotating flow in a channel owing to arbitrary conducting walls. Seth et al. [32] observed the Hall effect for the heat transfer phenomenon in ramped thermal temperature. Abbasi et al. [33] addressed the Hall effect on Jeffrey nanofluid caused by peristaltic transport.

The motivation for presenting the current flow model is the observation of the thermal impact of a hybrid nanofluid model for the slip flow of Casson fluid with applications of peristaltic phenomena [34–36]. The motivation for the consideration of the Casson fluid model is justified by the fact that it reports the shear thinning and shear thickening effects associated with human blood. The novel aspects of the current research are:

➢ The presentation of a mathematical model for the peristaltic transport of Casson fluid with the interaction of hybrid nanofluid containing the ferro nanoparticles and copper nanomaterials in a curved channel.
➢ The role of slip effects and Hall current is also observed.
➢ The highly nonlinear system of the obtained model is numerically solved with the ND-Solver.
➢ The physical thermal impact of hybrid nanoparticles is focused to control the blood flow properties. The current investigation presents novel applications for human blood flow, thermal systems, various engineering processes, extrusion systems, human endoscopy, the control of heating phenomena, chemical processes and biomedical applications [37–42].

2. Mathematical Modeling of Hybrid Nanofluid

Consider an unsteady base in a channel with a curved surface caused by 2-D flow, where the channel width is taken as 2*b*. The rheology of hybrid nanofluid in the curved region is due to peristaltic pumping. The complex sinusoidal waves with speed *c* are imposed on the walls of the conduit. In order to model the problem in the curved channel, curvilinear coordinates are incorporated instead of cylindrical coordinates. A sketch of the flow under conditions of the flow problem and coordinate system is presented in Figure 1. The transportation of fluid is chosen along the *S*-axis and the *X*-axis is chosen to be normal to the surface of the conduit. The radius of the channel is Λ and *O* is the center of the channel.
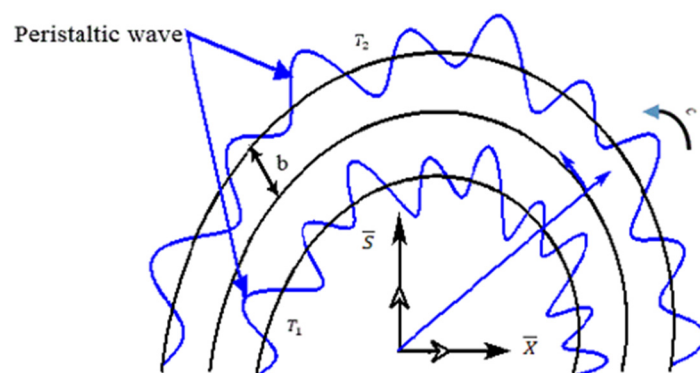

Figure 1. Flow illustration of model.

The mathematical expressions to describe the complex peristaltic waves are [34–36]:

$$\overline{H}_2\left(\overline{S},\overline{t}\right) = b + \overline{M}\left(\overline{S} - c\overline{t}\right) + \overline{\Phi}_1 \sin\left(\frac{2\sigma\pi}{\beta}\left(\overline{S} - c\overline{t}\right)\right) + \overline{\Phi}_2 \sin\left(\frac{2\omega\pi}{\beta}\left(\overline{S} - c\overline{t}\right)\right) \tag{1}$$

$$\overline{H}_1\left(\overline{S},\overline{t}\right) = -b - \overline{M}\left(\overline{S} - c\overline{t}\right) - \overline{\Phi}_1 \sin\left(\frac{2\sigma\pi}{\beta}\left(\overline{S} - c\overline{t}\right) + \sigma\epsilon\right) - \overline{\Phi}_2 \sin\left(\frac{2\omega\pi}{\beta}\left(\overline{S} - c\overline{t}\right) + \omega\epsilon\right), \tag{2}$$

with wavelength (β), non-uniform factor $(\overline{M})$, wave speed (c), phase difference (ϵ) and wave amplitudes (Φ_1, Φ_2). The tangential, radial and axial directions are denoted with $\overline{X}$, $\overline{Z}$ and $\overline{S}$, respectively. The observations for a straight channel are observed when the curvature of channel Λ approaches to ∞. The axial and radial velocity components are $\overline{U}_2$ and $\overline{U}_1$, respectively.

The contribution of magnetic force is taken in radial directions with Lorentz force:

$$\overline{F} = \overline{J_1} \times \overline{B} \tag{3}$$

The Hall current is:

$$\overline{J_1} + \frac{en_e}{B_0}\left(\overline{J_1} \times \overline{B}_,\right) = \sigma_{hnf}\left[\overline{V} \times \overline{B}\right] \tag{4}$$

having n_e (free electron density), e (electric charge) and σ_{hnf} (hybrid nanoparticles' electric conductivity). Writing Equation (4) with components:

$$\left.\begin{array}{r} J_{1r} = 0, \\ \frac{m\Lambda}{\overline{X}+\Lambda}J_{1z} + J_{1\theta} = 0, \\ -\frac{m\Lambda}{\overline{X}+\Lambda}J_{1\theta} + J_{1z} = -\frac{\sigma_{hnf}B_0\Lambda}{\overline{X}+\Lambda}\overline{U}_2, \end{array}\right\} \tag{5}$$

where, $m = en_e$ is the Hall parameter. In view of Equation (5):

$$J_{1\theta} = -\frac{\sigma_{hnf}B_0\Lambda^2}{\left(\overline{X}+\Lambda\right)^2}\overline{U}_2\left(\frac{m}{1+\left(\frac{m\Lambda}{\overline{X}+\Lambda}\right)^2}\right) \tag{6}$$

$$J_{1z} = \frac{\sigma_{hnf}B_0\Lambda}{\left(\overline{X}+\Lambda\right)}\overline{U}_2\left(\frac{1}{1+\left(\frac{m\Lambda}{\overline{X}+\Lambda}\right)^2}\right) \tag{7}$$

All defined flow assumptions lead to following governing system [34–36]:

$$\frac{\partial}{\partial\overline{X}}\left\{\left(\overline{X}+\Lambda\right)\overline{U}_1\right\} + \Lambda\frac{\partial\overline{U}_2}{\partial\overline{S}} = 0 \tag{8}$$

$$\rho_{hnf}\left(\frac{\partial\overline{U}_1}{\partial\overline{t}} + U_1\frac{\partial\overline{U}_1}{\partial\overline{X}} + \frac{\overline{U}_2\Lambda}{\overline{X}+\Lambda}\frac{\partial\overline{U}_1}{\partial\overline{S}} - \frac{\overline{U}_2^2}{\overline{X}+\Lambda}\right) = -\frac{\partial\overline{P}}{\partial\overline{X}} + \mu_{hnf}\left(1+\frac{1}{\gamma_1}\right)$$
$$\left(\frac{1}{\overline{X}+\Lambda}\frac{\partial}{\partial\overline{X}}\left(\left(\overline{X}+\Lambda\right)\frac{\partial\overline{U}_1}{\partial\overline{X}}\right) + \left(\frac{\Lambda}{\overline{X}+\Lambda}\right)^2\frac{\partial^2\overline{U}_1}{\partial\overline{S}^2} - \frac{2\Lambda}{\left(\overline{X}+\Lambda\right)^2}\frac{\partial\overline{U}_2}{\partial\overline{S}} - \frac{\overline{U}_1}{\left(\overline{X}+\Lambda\right)^2}\right) \tag{9}$$

$$\rho_{hnf}\left(\frac{\partial\overline{U}_2}{\partial\overline{t}} + \overline{U}_1\frac{\partial\overline{U}_2}{\partial\overline{X}} + \frac{\overline{U}_2\Lambda}{\overline{X}+\Lambda}\frac{\partial\overline{U}_2}{\partial\overline{S}} - \frac{\overline{U}_1\overline{U}_2}{\overline{X}+\Lambda}\right) = -\frac{\Lambda}{\overline{X}+\Lambda}\frac{\partial\overline{P}}{\partial\overline{S}} + \mu_{hnf}\left(1+\frac{1}{\gamma_1}\right)$$
$$\left(\frac{1}{\overline{X}+\Lambda}\frac{\partial}{\partial\overline{X}}\left(\left(\overline{X}+\Lambda\right)\frac{\partial\overline{U}_2}{\partial\overline{X}}\right) + \left(\frac{\Lambda}{\overline{X}+\Lambda}\right)^2\frac{\partial^2\overline{U}_2}{\partial\overline{S}^2} + \frac{2\Lambda}{\left(\overline{X}+\Lambda\right)^2}\frac{\partial\overline{U}_1}{\partial\overline{S}} - \frac{\overline{U}_2}{\left(\overline{X}+\Lambda\right)^2}\right) - \frac{\sigma_{hnf}B_0^2\Lambda^2}{\left(\overline{X}+\Lambda\right)^2}\overline{U}_2\left(\frac{1}{1+\left(\frac{m\Lambda}{\overline{X}+\Lambda}\right)^2}\right) \tag{10}$$

$$(\rho C_p)_{hnf}\left(\frac{\partial \overline{T}}{\partial \bar{t}} + \overline{U}_1 \frac{\partial \overline{T}}{\partial \overline{X}} + \frac{\overline{U}_2 \Lambda}{\overline{X} + \Lambda}\frac{\partial \overline{T}}{\partial \overline{S}}\right) = K_{hnf}\left(\frac{1}{\overline{X}+\Lambda}\frac{\partial}{\partial \overline{X}}\left((\overline{X}+\Lambda)\frac{\partial \overline{T}}{\partial \overline{X}}\right) + \left(\frac{\Lambda}{\overline{X}+\Lambda}\right)^2 \frac{\partial^2 \overline{T}}{\partial \overline{S}^2}\right) + \mu_{hnf}\left(1 + \frac{1}{\gamma_1}\right)$$

$$\left(2\left\{\left(\frac{\partial \overline{U}_1}{\partial \overline{X}}\right)^2 + \left(\frac{\Lambda}{\overline{X}+\Lambda}\frac{\partial \overline{U}_2}{\partial \overline{S}} + \frac{\overline{U}_1}{\overline{X}+\Lambda}\right)^2\right\} + \left(\frac{\partial \overline{U}_2}{\partial \overline{X}} + \frac{\Lambda}{\overline{X}+\Lambda}\frac{\partial \overline{U}_1}{\partial \overline{S}} - \frac{\overline{U}_2}{\overline{X}+\Lambda}\right)^2\right) + \frac{\sigma_{hnf}B_0^2 \Lambda^2}{(\overline{X}+\Lambda)^2 + (m\Lambda)^2}U_2^2. \tag{11}$$

with μ_{hnf} (viscosity), $(\rho C_p)_{hnf}$ (heating capacity), ρ_{hnf} (density), γ_1 (Casson factor) and K_{hnf} (thermal conductivity). Table 1 is organized in order to present the flow properties of the hybrid model.

Table 1. Hybrid nanofluid different consequences with mathematical forms [5].

Density	$\rho_{hnf} = (1-\alpha_1-\alpha_2)\rho_f + \alpha_1\rho_{s_1} + \alpha_2\rho_{s_2}.$
Viscosity	$\mu_{hnf} = \dfrac{\mu_f}{(1-\alpha_1-\alpha_2)^{2.5}}$
Effective heat capacity	$(\rho C_p)_{hnf} = (1-\alpha_1-\alpha_2)\rho_f(C_p)_f + \alpha_1\rho_{s_1}(C_p)_{s_1} + \alpha_2\rho_{s_2}(C_p)_{s_2}$
Thermal conductivity	$\dfrac{K_{hnf}}{K_f} = \dfrac{\dfrac{\alpha_1 K_{s_1} + \alpha_2 K_{s_2}}{\alpha_1 + \alpha_2} + 2K_f - 2K_f(\alpha_1+\alpha_2) + 2(\alpha_1 K_{s_1} + \alpha_2 K_{s_2})}{\dfrac{\alpha_1 K_{s_1} + \alpha_2 K_{s_2}}{\alpha_1 + \alpha_2} + 2K_f + K(\alpha_1+\alpha_2) - (\alpha_1 K_{s_1} + \alpha_2 K_{s_2})}$
Electric conductivity	$\dfrac{\sigma_{hnf}}{\sigma_{bf}} = \dfrac{\sigma_{s_1} + 2\sigma_{bf} - 2\alpha_2\left(\sigma_{bf} - \sigma_{s_1}\right)}{\sigma_{s_1} + 2\sigma_{bf} + \alpha_2\left(\sigma_{bf} - \sigma_{s_1}\right)}$ where $\sigma_{bf} = \dfrac{\sigma_{s_2} + 2\sigma_f - 2\alpha_1\left(\sigma_f - \sigma_{s_2}\right)}{\sigma_{s_2} + 2\sigma_f + \alpha_1\left(\sigma_f - \sigma_{s_2}\right)}\sigma_f$

Changing the problem from fixed to waves frame by introducing the following transportations:

$$\bar{s} = \overline{S} - c\bar{t}, \overline{X} = \bar{x}, \overline{u}_1 = \overline{U}_1, \overline{u}_2 = \overline{U}_2 - c, \overline{P} = \bar{p} \tag{12}$$

Following the above transformations, Equations (9)–(12) become:

$$\frac{\partial}{\partial \bar{x}}\{(\bar{x}+\Lambda)\overline{u}_1\} + \Lambda \frac{\partial \overline{u}_2}{\partial \bar{s}} = 0, \tag{13}$$

$$\rho_{hnf}\left(-c\frac{\partial \overline{u}_1}{\partial \bar{s}} + u_1\frac{\partial \overline{u}_1}{\partial \bar{x}} + \frac{(\overline{u}_2+c)\Lambda}{\overline{X}+\Lambda}\frac{\partial \overline{u}_1}{\partial \bar{s}} - \frac{(\overline{u}_2+c)^2}{\bar{x}+\Lambda}\right) = -\frac{\partial \bar{p}}{\partial \bar{x}} + \mu_{hnf}\left(1+\frac{1}{\gamma_1}\right)$$

$$\left(\frac{1}{\bar{x}+\Lambda}\frac{\partial}{\partial \bar{x}}\left((\bar{x}+\Lambda)\frac{\partial \overline{u}_1}{\partial \bar{x}}\right) + \left(\frac{\Lambda}{\bar{x}+\Lambda}\right)^2\frac{\partial^2 \overline{u}_1}{\partial \bar{s}^2} - \frac{2\Lambda}{(\bar{x}+\Lambda)^2}\frac{\partial \overline{u}_2}{\partial \bar{s}} - \frac{u_1}{(\bar{x}+\Lambda)^2}\right) \tag{14}$$

$$\rho_{hnf}\left(-c\frac{\partial \overline{u}_2}{\partial \bar{s}} + \overline{u}_1\frac{\partial \overline{u}_2}{\partial \bar{x}} + \frac{(\overline{u}_2+c)\Lambda}{\bar{x}+\Lambda}\frac{\partial \overline{u}_2}{\partial \bar{s}} - \frac{\overline{u}_1(\overline{u}_2+c)}{\bar{x}+\Lambda}\right) = -\frac{\Lambda}{\bar{x}+\Lambda}\frac{\partial \bar{p}}{\partial \bar{s}} + \mu_{hnf}\left(1+\frac{1}{\gamma_1}\right)$$

$$\left(\frac{1}{\bar{x}+\Lambda}\frac{\partial}{\partial \bar{x}}\left((\bar{x}+\Lambda)\frac{\partial \overline{u}_2}{\partial \bar{x}}\right) + \left(\frac{\Lambda}{\bar{x}+\Lambda}\right)^2\frac{\partial^2 \overline{u}_2}{\partial \bar{s}^2} + \frac{2\Lambda}{(\bar{x}+\Lambda)^2}\frac{\partial \overline{u}_1}{\partial \bar{s}} - \frac{\overline{u}_2+c}{(\bar{x}+\Lambda)^2}\right) - \frac{\sigma_{hnf}B_0^2\Lambda^2}{(\bar{x}+\Lambda)^2}(\overline{u}_2+c)\left(\frac{1}{1+\left(\frac{m\Lambda}{\bar{x}+\Lambda}\right)^2}\right) \tag{15}$$

$$(\rho C_p)_{hnf}\left(\overline{u}_1\frac{\partial \overline{T}}{\partial \bar{x}} + \frac{(\overline{u}_2+c)\Lambda}{\bar{x}+\Lambda}\frac{\partial \overline{T}}{\partial \bar{s}}\right) = K_{hnf}\left(\frac{1}{\bar{x}+\Lambda}\frac{\partial}{\partial \bar{x}}\left((\bar{x}+\Lambda)\frac{\partial \overline{T}}{\partial \bar{x}}\right) + \left(\frac{\Lambda}{\bar{x}+\Lambda}\right)^2\frac{\partial^2 \overline{T}}{\partial \bar{s}^2}\right) + \mu_{hnf}\left(1+\frac{1}{\gamma_1}\right)$$

$$\left(2\left\{\left(\frac{\partial \overline{u}_1}{\partial \bar{x}}\right)^2 + \left(\frac{\Lambda}{\overline{X}+\Lambda}\frac{\partial(\overline{u}_2)}{\partial \bar{s}} + \frac{\overline{u}_1}{\bar{x}+\Lambda}\right)^2\right\} + \left(\frac{\partial(\overline{u}_2)}{\partial \bar{x}} + \frac{\Lambda}{\bar{x}+\Lambda}\frac{\partial \overline{u}_1}{\partial \bar{s}} - \frac{(\overline{u}_2+c)}{\bar{x}+\Lambda}\right)^2\right) + \frac{\sigma_{hnf}B_0^2\Lambda^2}{(\bar{x}+\Lambda)^2 + (m\Lambda)^2}(\overline{u}_2+c)^2, \tag{16}$$

Now we use the dimensionless variables [34–36]:

$$s = \frac{2\pi\bar{s}}{\beta}, \eta = \frac{\bar{x}}{b}, u_1 = \frac{\overline{u}_1}{c}, u_2 = \frac{\overline{u}_2}{c}, \delta = \frac{2\pi b}{\beta}, h = \frac{\overline{H}}{b}, Re = \frac{\rho_f cb}{\mu_f}, k = \frac{\Lambda}{b}, p = \frac{2\pi b^2}{\beta \mu_f c}\bar{p},.$$

$$\Phi_i = \frac{\overline{\Phi_i}}{b}, i = 1, 2, m_1 = \frac{\beta \overline{M}}{b}, \ Ha = \sqrt{\frac{\sigma_f}{\mu_f}} B_0 b, \ \theta = \frac{\overline{T} - T_1}{T_2 - T_1}, \ Ec = \frac{c^2}{C_f(T_2 - T_1)}, \ Pr = \frac{\mu_f C_f}{K_f}, .$$

$$Br = PrEc,$$

with η (radial direction component), u_1 (radial velocity), s (axial component), u_2 (axial velocity), Re (Reynolds constant), Pr (Prandtl constant), k (dimensionless curvature), Ha (Hartmann number), δ (wave number), M (non-uniform parameter), Ec (Eckert number) and Br (Brinkman number). Using stream functions defining as $u_1 = \delta(\Lambda/\eta + \Lambda)\partial\psi/\partial s$ and $u_2 = -\partial\psi/\partial\eta$ and implementing the smaller Reynolds assumptions, the rest of equations take the form [34–36]:

$$\frac{\partial p}{\partial \eta} = 0. \tag{17}$$

$$\frac{\partial p}{\partial s} = \frac{1}{k(k+\eta)} \frac{1}{(1-\alpha_1-\alpha_2)^{2.5}} \left(1 + \frac{1}{\gamma_1}\right) \frac{\partial}{\partial \eta}\left((\eta+k)\left(1 - \frac{\partial \psi}{\partial \eta}\right) + (\eta+k)^2 \frac{\partial^2 \psi}{\partial \eta^2}\right)$$
$$-C_1 \frac{Ha^2 k^2}{(\eta+k)^2 + (mk)^2}\left(1 - \frac{\partial \psi}{\partial \eta}\right), \tag{18}$$

$$C_2\left(\frac{\partial^2 \theta}{\partial \eta^2} + \frac{1}{\eta+k}\frac{\partial \theta}{\partial \eta}\right) + \frac{Br}{(1-\alpha_1-\alpha_2)^{2.5}}\left(1 + \frac{1}{\gamma_1}\right)\left(\frac{\partial^2 \psi}{\partial \eta^2} + \frac{1}{\eta+k}\left(1 - \frac{\partial \psi}{\partial \eta}\right)\right)^2$$
$$+\frac{k^2 Br Ha^2 C_1}{(\eta+k)^2 + (mk)^2}\left(1 - \frac{\partial \psi}{\partial \eta}\right)^2 = 0. \tag{19}$$

with the copper nanoparticles' volume fraction (α_1) and ferro nanomaterials volume fraction of α_2. Moreover $C_1 = \frac{\sigma_{s_1} + 2\sigma_{bf} - 2\alpha_2\left(\sigma_{bf} - \sigma_{s_1}\right)}{\sigma_{s_1} + 2\sigma_{bf} + \alpha_2\left(\sigma_{bf} - \sigma_{s_1}\right)}$, where $\sigma_{bf} = \frac{\sigma_{s_2} + 2\sigma_f - 2\alpha_1\left(\sigma_f - \sigma_{s_2}\right)}{\sigma_{s_2} + 2\sigma_f + \alpha_1\left(\sigma_f - \sigma_{s_2}\right)}\sigma_f$ and

$$C_2 = \frac{K_{hnf}}{K_f} = \frac{\frac{\alpha_1 K_{s_1} + \alpha_2 K_{s_2}}{\alpha_1 + \alpha_2} + 2K_f - 2K_f(\alpha_1 + \alpha_2) + 2\left(\alpha_1 K_{s_1} + \alpha_2 K_{s_2}\right)}{\frac{\alpha_1 K_{s_1} + \alpha_2 K_{s_2}}{\alpha_1 + \alpha_2} + 2K_f + K(\alpha_1 + \alpha_2) - \left(\alpha_1 K_{s_1} + \alpha_2 K_{s_2}\right)}.$$

The boundary conditions in terms of stream function [34–36]:

$$\psi = -\frac{q}{2}, \frac{\partial \psi}{\partial \eta} + \beta_1\left(1 + \frac{1}{\gamma_1}\right)\frac{1}{(1-\alpha_1-\alpha_2)^{2.5}}\left(-\frac{\partial^2 \psi}{\partial \eta^2} - \frac{1}{\eta+k}\left(1 - \frac{\partial \psi}{\partial \eta}\right)\right) = 1, \theta = 1 \tag{20}$$

$$\text{at } \eta = h_2 = 1 + m_1 s + \Phi_1 \sin(\sigma s) + \Phi_2 \sin(\omega s) \tag{21}$$

$$\psi = \frac{q}{2}, \frac{\partial \psi}{\partial \eta} - \beta_1\left(1 + \frac{1}{\gamma_1}\right)\frac{1}{(1-\alpha_1-\alpha_2)^{2.5}}\left(-\frac{\partial^2 \psi}{\partial \eta^2} - \frac{1}{\eta+k}\left(1 - \frac{\partial \psi}{\partial \eta}\right)\right) = 1, \theta = 0 \tag{22}$$

$$\text{at } \eta = h_1 = -1 - m_1 s - \Phi_1 \sin(\sigma(s+\epsilon) - \Phi_2 \sin(\omega(s+\epsilon)) \tag{23}$$

For mean flow:

$$\Omega_1 = q + 2 \tag{24}$$

Defining q as:

$$q = \int_{-h}^{h} \frac{\partial \psi}{\partial \eta} d\eta, \tag{25}$$

The fluctuation in pressure rise, wall shear force and heating transfer coefficient near the lower surface wall and upper surface is:

$$\Delta p = \int_0^{2\pi} \frac{dp}{dx} dx \tag{26}$$

$$C_f = -\frac{\partial h_1}{\partial s}\frac{\partial^2 \psi}{\partial \eta^2}\bigg|_{h_1} \tag{27}$$

$$Z_1 = \frac{\partial h_2}{\partial s}\frac{\partial \theta}{\partial \eta}\bigg|_{h_2} \tag{28}$$

3. Solution of the Problem

After eliminating pressure for Equations (17) and (18), the shooting method with built-in ND solver is applied. This scheme is well-known and is not presented in detail here. Table 2 interprets the numerical values of density, thermal conductivity, specific heat and electrical conductivity.

Table 2. The properties of ferro nanoparticles, copper and human blood [5,16].

Material	Cu	Blood	Fe_3O_4
$\rho \; (kg/m^3)$	8933	1063	5200
$K \; (W/mk)$	401	0.492	6
$C \; (J/kgK)$	385	3594	670
$\sigma \; (S/m)$	5.96×10^7	0.8	25,000

4. Discussion

This section claims some physical importance of the parameters for different flow regimes. For this task, the values are parameters which are defined as $\sigma = 1$, $m_1 = 0.2$, $\omega = 1$ and $\epsilon = \pi$.

4.1. Axial Velocity Profile

Figure 2 is the graphical representation of the axial velocity against the several involved parameters for non-similar values of flow rate q, i.e., $q = 0.1$ and $q = -5.0$. The velocity profile is plotted and examined under the influence of both the slip and non-Newtonian rheology of the nanofluid. From Figure 2a, it is clear that the velocity of the hybrid nanofluid declines at the central line of the channel by boosting the solid volume fraction of Cu nanoparticles and near the walls of the channel the velocity rises; this behavior is same for several values of q. Physically, these results show that the solid volume fraction plays a dynamic role in the transport of blood near the lubricated walls of curved micro-vascular conduits in the presence of hybrid nanoparticles. The solid volume fraction of copper nanoparticles can also play a key role in the regulation of blood in diseased arteries with lubricated walls. A similar trend is observed in Figure 2b for the axial velocity by boosting the solid volume fraction of Fe_3O_4 nanoparticles for both $q = 0.1$ and $q = -5.0$. This indicates that due to the interaction of the nanoparticles, which control the thermal transport near the micro channel, there is a decrease in velocity in the center of the channel, and due to the slip features at the walls, the velocity rises. Figure 2c is plotted to analyze the change in the axial velocity component due to increasing fluctuation of the Hartmann number. The reduced results are observed in the upper regime when enhancing values are being assigned to the Hartmann number. However, a rising velocity in the lower regime is observed for the same Hartmann constant variation. The change in the Hartmann number against the axial velocity is described via Figure 2d. Reduced velocity in the core of the channel is observed. As a result, a depressive velocity trend occurs and the velocity fluctuates toward the upper regime of the channel. The reduction in velocity flow is due to the application of magnetic force which results in a resistive Lorentz force. The control of velocity due to m_1 has been noted in Figure 2e. The enhanced change in hybrid nanofluid movement against m_1 in the core regime is noticed. Moreover, the channel diameter begins to decrease when larger measurements are assigned to m_1. Figure 2f presents important observations of the change in velocity caused by the impact of curvature k. The results are further observed for an infinite range of curvature. The response of velocity is similar for non-similar values of flow rate q.
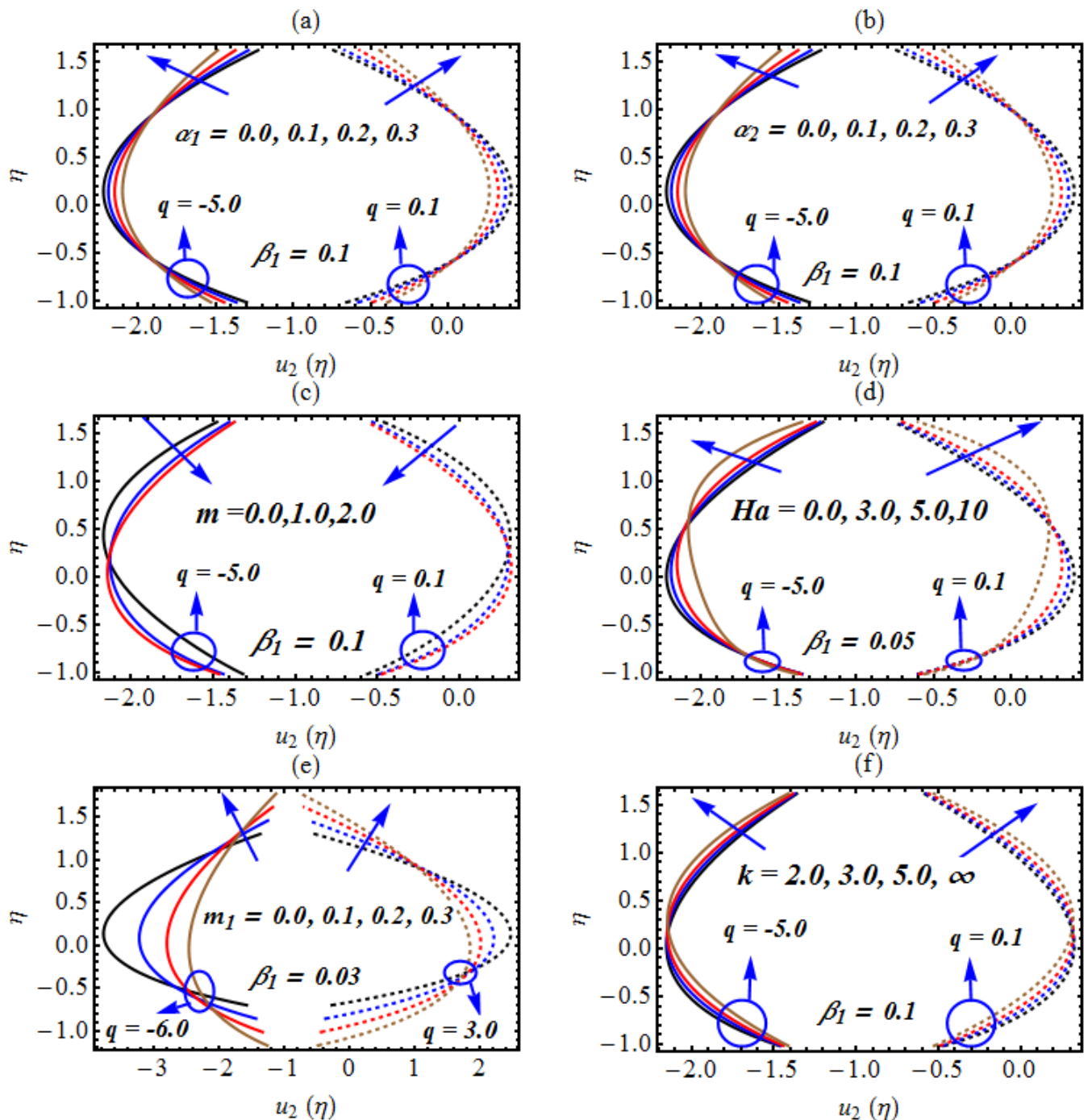
Figure 2. (**a–f**): (**a**) Change in $u_2(\eta)$ for α_1, (**b**) change in $u_2(\eta)$ for α_2, (**c**) change in $u_2(\eta)$ for m, (**d**) change in $u_2(\eta)$ for Ha, (**e**) change in $u_2(\eta)$ for m_1, (**f**) change in $u_2(\eta)$ for m_1/.

4.2. Temperature Profile

The results described in Figure 3a present the trends of temperature profile $\theta(\eta)$ due to the Casson fluid parameter for Cu/blood nanofluid and hybrid nanofluid [34–36]. The noted observations reveal that both Cu/blood nanofluid and hybrid nanofluid are a decreasing function of the Casson parameter. As the Casson parameter increases, the behavior of the fluid approach that of viscous fluid, so for viscous fluid the temperature is minimal and for the Casson fluid the temperature is maximal. As the non-Newtonian character is added, the resistance between the layers of fluid rises, increasing the internal kinetic energy of the colloidal suspension. As a result, the enhancing temperature rate is deduced [34–36]. The same nature of temperature results from enrolling the change in the velocity slip constant

(Figure 2b). The Hall current reduces the role of Lorentz force as seen in Figure 2c. The graphical observations in Figure 2d demonstrate an increase in the thermal rate caused by an increasing Hartmann number. An improvement in the thermal performance of the copper–blood suspension is observed due to Lorentz force. Similarly, an improved heat transfer phenomenon is noted for ferro-copper nanoparticles. Such results may have important implications for applications within ferromagnetic materials and industrial processes. An increase in temperature is visualized when the non-uniformity of the channel increases (Figure 2e). Therefore, the non-uniformity of the surface geometry plays an important role in the thermal transmission of various processes. Figure 2f demonstrates a low temperature rate for an increasing curvature constant.
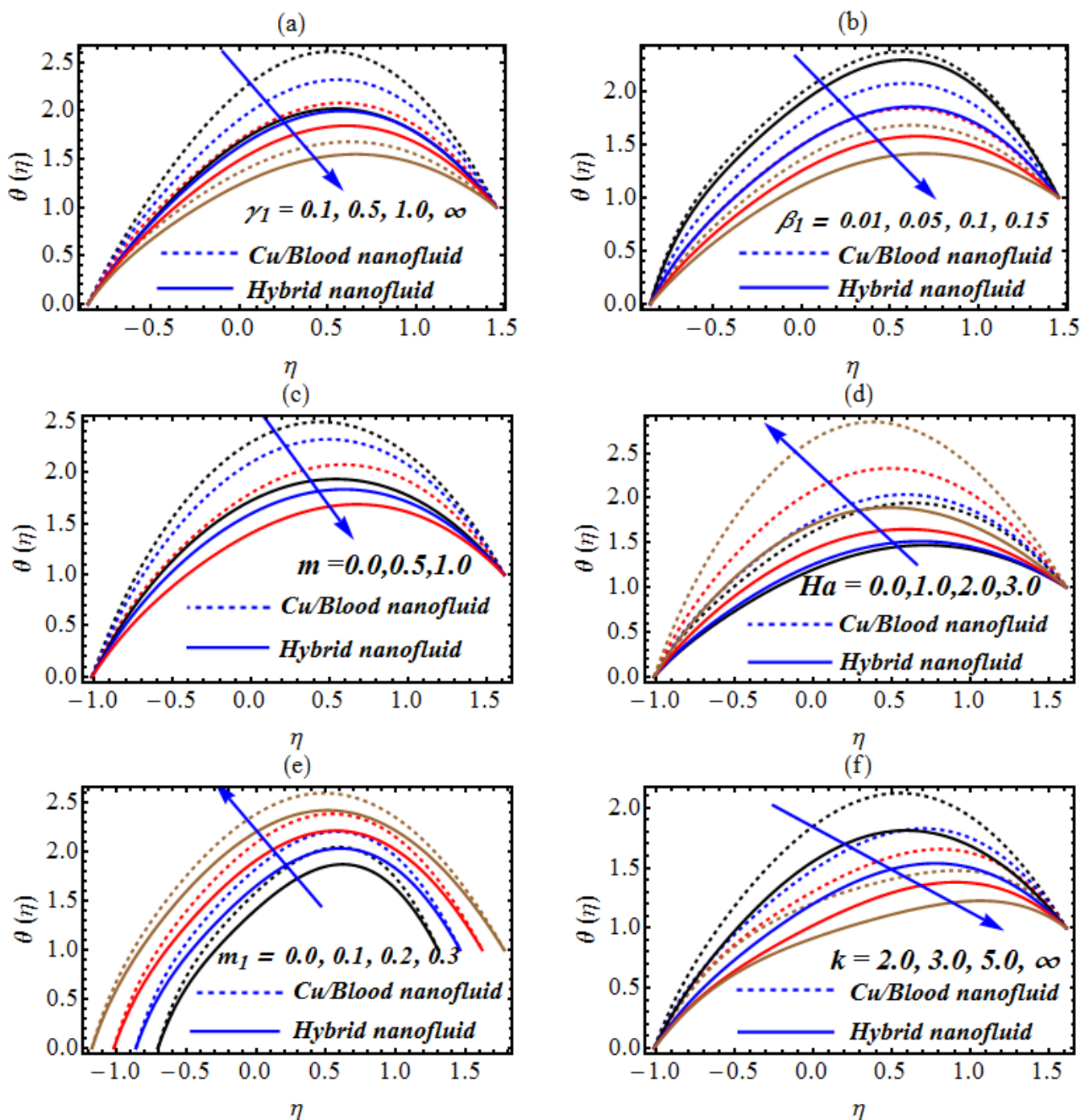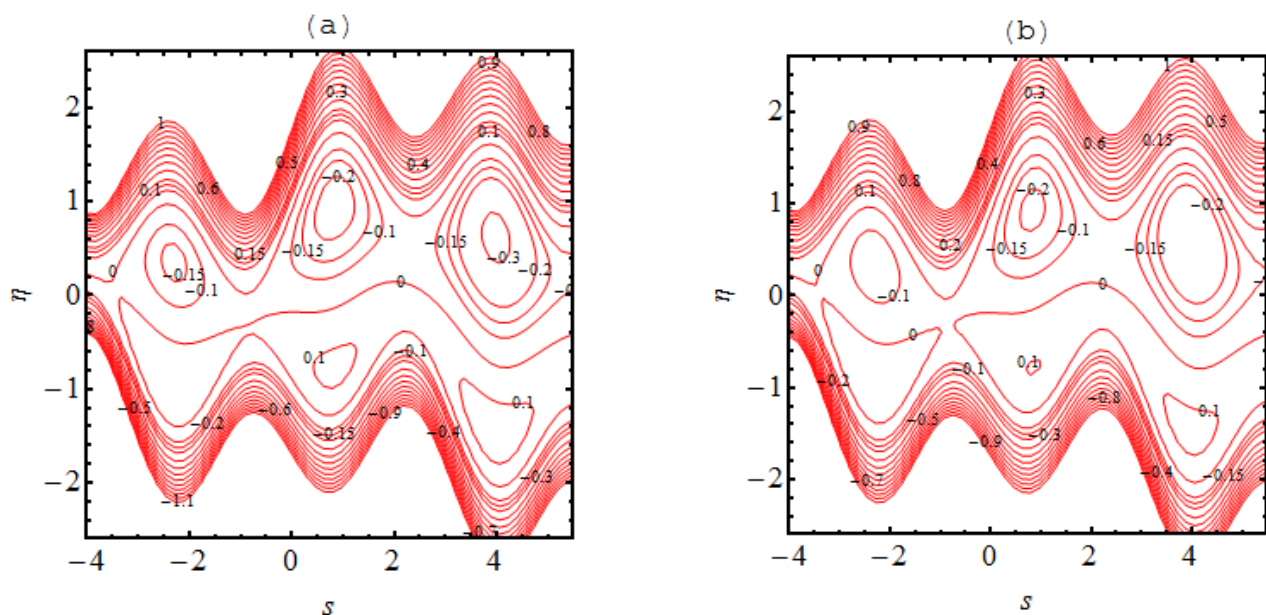

Figure 3. (**a**–**f**): (**a**) Change in θ for γ_1 (**b**) change in θ for β_1, (**c**) change in θ for m, (**d**) change in θ for Ha, (**e**) change in θ for m_1 and (**f**) change in θ for k.

4.3. Trapping Phenomena

In many situations the boluses of fluid are generated in the flow regimes which are enclosed by streamlines; this occurrence is referred to as trapping phenomena. This trapping is an important rheological feature related to the dynamics of the bolus under various circumstances. A wavy streamlined shape is produced in the vicinity of the walls on both halves of the channel due to the complex wave pattern on the wall. Furthermore, the flow structure of the trapping phenomena can be discussed and predicted due to the non-uniformity of the flow patterns. Figures 4–7 demonstrate the significance of α_1, α_2, Ha, m and m_1. The nature of the bolus is noted for the parameters defined in Figure 4. A smaller bolus size is exhibited, which disappears in the upper channel regime when the volume fraction rate increases. From Figures 4b, 5b, 6b and 7b, larger bolus size in associated to the increasing volume fraction rate. Such a trend is due to the addition of solid nanoparticles to the base liquid. From Figure 5, it can be observed that the concentration of the bolus plays no role on either of the channel surfaces. The appearance of the bolus in the channel is observed without the participation of the magnetic phenomenon. Actually, the fluid trapped towards the wall of the channel and the flow patterns near the walls develop under strong magnetic force. Figure 6 shows the effect of the onset of the Hall factor on the trapping phenomenon; the opposite effect is noted for the Hall parameter. From Figure 7, the bolus is seen to disappear inside the channel when movement is observed in the uniform and non-uniform channel regimes.
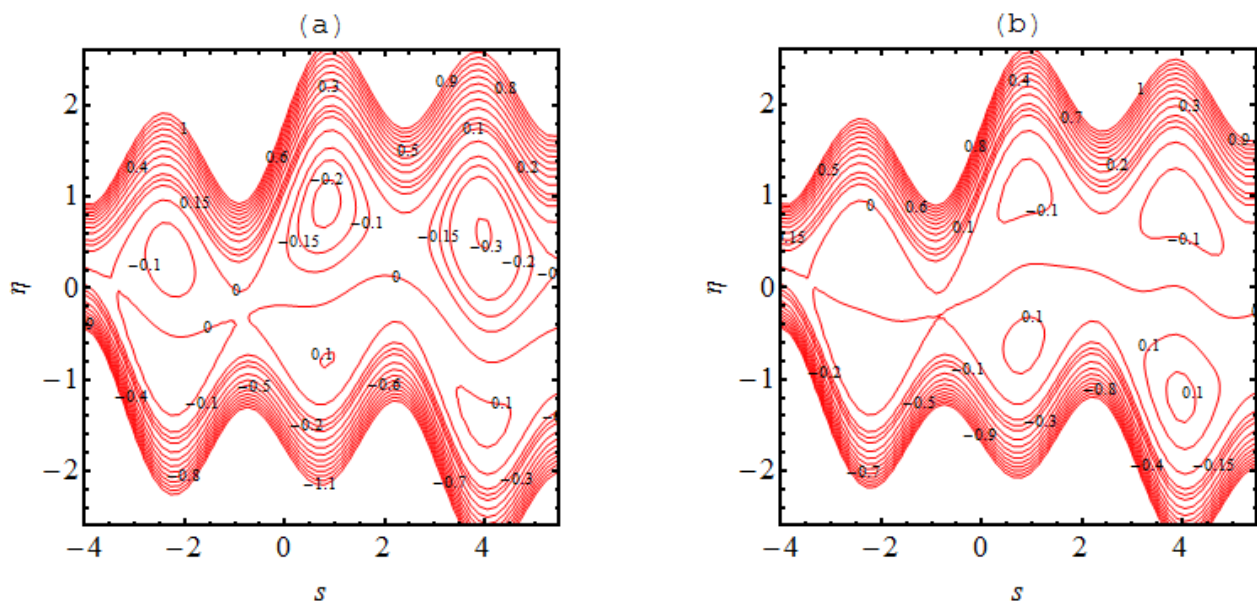

Figure 4. Stream lines for (**a**) $\alpha_1 = 0.0$ and (**b**) $\alpha_1 = 0.1$ the other parameters are $Ha = 3.0$, $k = 3.0$, $m = 2.0$, $q = -0.1$, $\gamma_1 = 1.0$, $\beta_1 = 0.1$.

4.4. Pressure Rise

Figure 8a,b is presented to visualize the change in the pumping phenomenon against the nanomaterials' volume fraction. Owing to the larger nanomaterial concentration, the increment in pressure is observed, while the contrary trend is noticed in the co-pumping regime. Moreover, slightly larger pressure distribution is results from copper nanoparticles. Such results are significant for roller pumping design due to curvature. Figure 8c,d demonstrates the phenomenon of pressure change for the Hartmann number and the Hall factor. The enhancing pressure gradient is observed in the pumping core while the decrease is noted in the co-pumping zone.

Figure 5. Stream lines for (**a**) $Ha = 0.0$ and (**b**) $Ha = 3.0$ the other parameters are $\alpha_1 = 0.05$, $k = 3.0$, $m = 2.0$, $q = -0.1$ and $\alpha_2 = 0.1$.
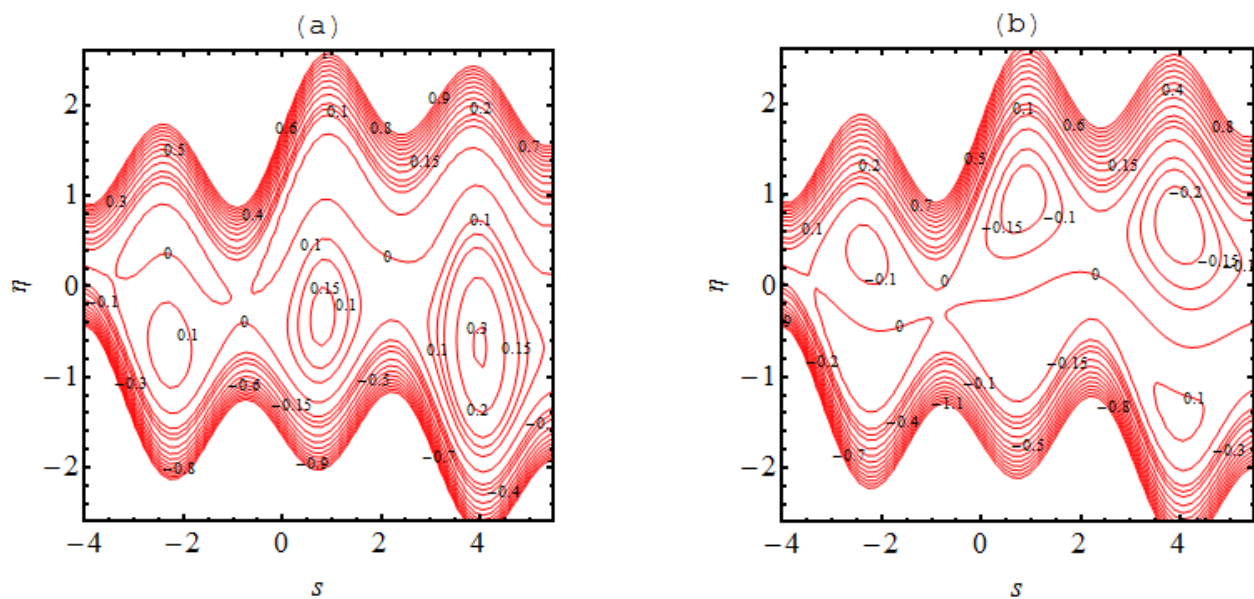

Figure 6. Stream lines for (**a**) $m = 0.0$ and (**b**) $m = 2.0$ the other parameters are $\alpha_1 = 0.05$, $k = 3.0$, $Ha = 3.0$, $q = -0.1$ and $\alpha_2 = 0.1$.

4.5. Heat Transfer Coefficient and Wall Shear Force

The numerical claims are listed in Table 3 to observe the change in heat transfer coefficient for copper nanoparticles ($\alpha_1 = 0.1, \alpha_2 = 0.0$) and hybrid nanofluid ($\alpha_1 = 0.1, \alpha_2 = 0.2$). The analysis is investigated for the hybrid nanofluid model and the blood/copper nanofluid suspension. An increase in the heat transfer coefficient is noted upon enlarging the Hartmann factor. However, the larger transmission of energy is noted for the copper–blood decomposition. The role of the slip factor controls the heating phenomenon for both models. Observations of the decrement when varying the Hall parameter yield results. For the blood–copper model, the heat transfer factor increases for the Brinkman number as well as for the hybrid nanofluid, both with the no-slip mechanism and by entertaining the slip factor. Moreover, the increasing trend in the curved channel is noted. From Table 4, the numerical trend of the wall shear force increases for the Hartmann constant for all models.

However, the low wall shear results are determined for the hybrid model. The Hall current factor and curvature constant present decreasing changes for the wall shear quantity.
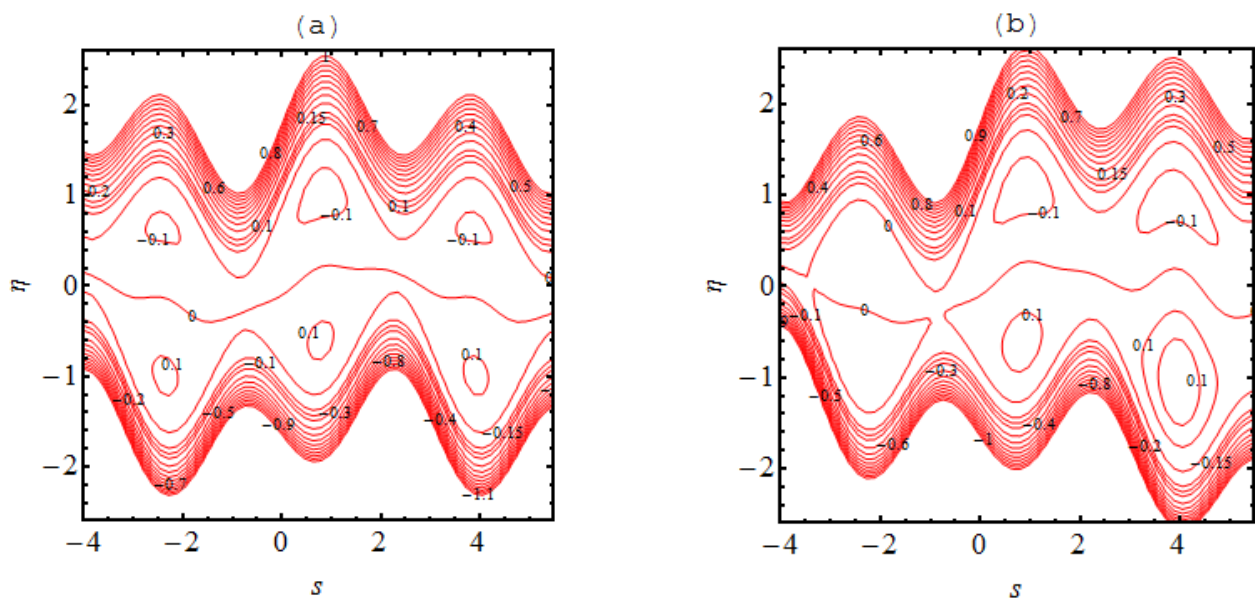

Figure 7. Stream lines for (**a**) $m_1 = 0.0$ and (**b**) $m_1 = 0.1$ where the other parameters are $\alpha_2 = 0.1$, $k = 3.0$, $Ha = 3.0$, $q = -0.1$, $m = 1.0$ and $\alpha_1 = 0.05$.
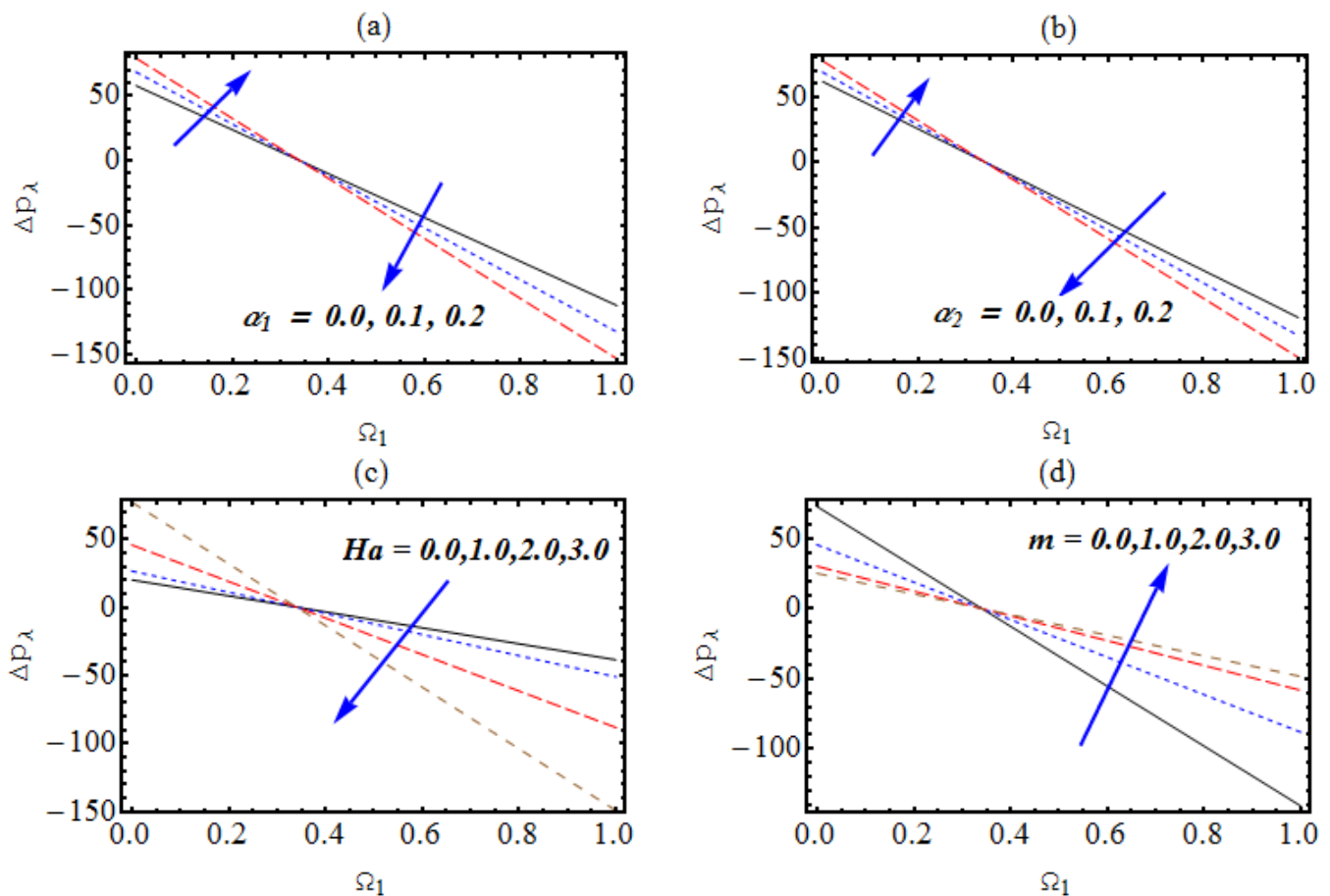

Figure 8. (**a**–**d**): (**a**) Change in pressure due to α_1, (**b**) change in pressure due to α_2, (**c**) change in pressure due to Ha (**d**) change in pressure due to m.

Table 3. Variation of heat transfer coefficient with $\gamma_1 = 1.0$ and $q = -0.2$.

Ha	m	Br	k	$\beta_1 = 0.0$		$\beta_1 = 0.1$	
				Cu Nanofluid	Hybrid Nanofluid	Cu Nanofluid	Hybrid Nanofluid
0.0	1.0	1.0	3.0	1.946431	1.803762	1.313924	1.305188
1.0				1.947308	1.804217	1.314652	1.305564
2.0				1.949939	1.805583	1.316832	1.306690
	0.0			1.952836	1.807087	1.319297	1.307965
	1.0			1.949939	1.805583	1.316832	1.306690
	2.0			1.947920	1.804535	1.315149	1.305820
		0.0		1.283249	1.283249	1.283249	1.283249
		2.0		2.56784366	2.28255142	1.30959600	1.290532
		4.0		3.85243826	3.28185379	1.33594274	1.29781534
			2.5	1.95869391	1.81494916	1.32416001	1.31492136
			5.0	1.92554637	1.78290025	1.29642262	1.28689076
			∞	1.88993547	1.74844033	1.26657588	1.25666942

Table 4. Change in skin friction with $\gamma_1 = 1.0$ and $q = -0.2$.

Ha	m	k	$\beta_1 = 0.0$		$\beta_1 = 0.1$	
			Cu Nanofluid	Hybrid Nanofluid	Cu Nanofluid	Hybrid Nanofluid
0.0	1.0	3.0	1.64793574	1.647935744	0.23902529	0.144332354
1.0			1.64825439	1.64814824	0.23902712	0.14433235
2.0			1.64921003	1.64878559	0.23903264	0.14433235
	0.0		1.65017632	1.64943017	0.23899158	0.14431076
	1.0		1.64921003	1.64878559	0.23903264	0.14433236
	2.0		1.64849017	1.64830548	0.23903597	0.14433582
		2.5	1.65630099	1.65612141	0.24164339	0.14724496
		5.0	1.63224142	1.63204609	0.23360486	0.13824367
		∞	1.60630293	1.60609039	0.22491558	0.12840275

5. Conclusions

The peristatic pumping-based blood flow with applications of hybrid nanofluid is studied in a curved channel. The determination of heat transfer is observed in ferro nanoparticles and copper nonmaterial. Additionally, the importance of the Hall factor contributes to make the model comprehensive. The significance of various flow parameters for velocity, heat transfer coefficients and pumping phenomena are visualized. The mains results are concluded as:

❖ The declining change in velocity associated with the larger Lorentz force is exhibited.
❖ Upon enhancing the Hall parameter, the role of magnetic force is controlled.
❖ The change in the non-uniformity of a curved surface and the increment in the rate of velocity are observed.
❖ A reduction in temperature results from a larger nanoparticle volume fraction.
❖ The heat transfer is increased for the curved configuration while lower results are noted for the planner channel.
❖ In both regimes of the symmetric channel, the disappearance of bolus trapping due to magnetic force is noted.

❖　　A progressive skin friction for hybrid nanofluid at low scales is given for Lorentz force.

References

1. Choi, S.U.; Eastman, J.A. Enhancing thermal conductivity of fluids with nanoparticles. *ASME-Publ.-Fed* **1995**, *231*, 99–106.
2. Buonigiorno, J. Convective transport in nanofluids. *J. Heat Transf.* **2010**, *128*, 240–250. [CrossRef]
3. Sui, J.; Zheng, L.; Zhang, X. Boundary layer heat and mass transfer with cattaneo christov double-diffusion in upper-convected maxwell nanofluid past a stretching sheet with slip velocity. *Int. J. Therm. Sci.* **2016**, *104*, 461–468. [CrossRef]
4. Sandeep, N.; Animasaun, I.I. Heat transfer in wall jet flow of magnetic-nanofluids with variable magnetic field. *Alex. Eng. J.* **2017**, *56*, 263–269. [CrossRef]
5. Afridi, M.I.; Qasim, M.; Khan, N.A.; Hamdani, M. Heat transfer analysis of Cu–Al_2O_3–water and Cu–Al_2O_3–kerosene oil hybrid nanofluids in the presence of frictional heating: Using 3-stage lobatto IIIA formula. *J. Nanofluids* **2019**, *8*, 885–891. [CrossRef]
6. Khan, S.U.; Waqas, H.; Bhatti, M.M.; Imran, M. Bioconvection in the rheology of magnetized couple stress nanofluid featuring activation energy and Wu's slip. *J. Non-Equilib. Thermodyn.* **2020**, *45*, 81–95. [CrossRef]
7. Kumar, A.; Tripathi, R.; Singh, R. Simultaneous effects of nonlinear thermal radiation and joule heating on the flow of williamson nanofluid with entropy generation. *Physica A* **2020**, *551*, 123972. [CrossRef]
8. Khan, S.U.; Shehzad, S.A.; Ali, N. Bioconvection flow of magnetized Williamson nanoliquid with motile organisms and variable thermal conductivity. *Appl. Nanosci.* **2020**, *10*, 3325–3336. [CrossRef]
9. Mondal, S.K.; Pal, D. Computational analysis of bioconvective flow of nanofluid containing gyrotactic microorganisms over a nonlinear stretching sheet with variable viscosity using HAM. *J. Comput. Des. Eng.* **2020**, *7*, 251–267. [CrossRef]
10. Ahmad, S.; Ashraf, M.; Ali, K. Nanofluid flow comprising gyrotactic microorganisms through a porous medium. *J. Appl. Fluid Mech.* **2020**, *13*, 1539–1549.
11. Makinde, O.D.; Khan, Z.; Khan, W.; Tshehla, M. Magneto-hemodynamics of nanofluid with heat and mass transfer in a slowly varying symmetrical channel. *Int. J. Eng. Res. Afr.* **2017**, *28*, 118–141. [CrossRef]
12. Das, S.; Tarafdar, B.; Jana, R.N.; Makinde, O.D. Influence of wall conductivities on a fully developed mixed-convection magneto-hydrodynamic nanofluid flow in a vertical channel. *J. Eng. Phys. Thermophys.* **2018**, *91*, 784–796. [CrossRef]
13. Mandal, P.K.; Singha, A.K.; Kumar, B.; Seth, G.S.; Sarkar, S. Analysis of unsteady magnetohydrodynamic 3-D rotating flow and transfer of heat in carbon nanotube-water nanofluid: An engineering application. *J. Nanofluids* **2022**, *11*, 204–213. [CrossRef]
14. Zhang, L.; Puneeth, V.; Ijaz Khan, M.; El-Zahar, E.R.; Manjunath, N.; Shah, N.A.; Chung, J.D.; Khan, S.U.; Khan, M.I. Applications of bioconvection for tiny particles due to two concentric cylinders when role of Lorentz force is significant. *PLoS ONE* **2022**, *17*, e0265026. [CrossRef]
15. Chu, Y.M.; Khan, N.; Khan, M.I.; Al-Khaled, K.; Abbas, N.; Khan, S.U.; Hashmi, M.S.; Qayyum, S.; Kadry, S. Thermophoresis particle deposition analysis for nonlinear thermally developed flow of Magneto-Walter's B nanofluid with buoyancy forces. *Alex. Eng. J.* **2021**, *60*, 1851–1860. [CrossRef]
16. Wahid, N.S.; Arifin, N.M.; Khashi'ie, N.S.; Pop, I. Marangoni hybrid nanofluid flow over a permeable infinite disk embedded in a porous medium. *Int. Commun. Heat Mass Transf.* **2021**, *126*, 105421. [CrossRef]
17. Almaneea, A. Thermal analysis for ferromagnetic fluid with hybrid nano-metallic structures in the presence of Forchheirmer porous medium subjected to a magnetic dipole. *Case Stud. Therm. Eng.* **2021**, *26*, 100961. [CrossRef]
18. Mousavi, S.M.; Rostami, M.N.; Yousefi, M.; Dinarvand, S.; Pop, I.; Sheremet, M.A. Dual solutions for casson hybrid nanofluid flow due to a stretching/shrinking sheet: A new combination of theoretical and experimental models. *Chin. J. Phys.* **2021**, *71*, 574–588. [CrossRef]
19. Khan, U.; Zaib, A.; Ishak, A.; Bakar, S.A. Time-dependent blasius–Rayleigh–Stokes flow conveying hybrid nanofluid and heat transfer induced by non-Fourier heat flux and transitive magnetic field. *Case Stud. Therm. Eng.* **2021**, *26*, 101151. [CrossRef]

20. Madhukesh, J.K.; Kumar, R.N.; Gowda, R.P.; Prasannakumara, B.C.; Ramesh, G.K.; Khan, M.I.; Khan, S.U.; Chu, Y.M. Numerical simulation of AA7072-AA7075/water-based hybrid nanofluid flow over a curved stretching sheet with Newtonian heating: A non-Fourier heat flux model approach. *J. Mol. Liq.* **2021**, *335*, 116103. [CrossRef]

21. Rashid, U.; Liang, H.; Ahmad, H.; Abbas, M.; Iqbal, A.; Hamed, Y.S. Study of (Ag and TiO2)/water nanoparticles shape effect on heat transfer and hybrid nanofluid flow toward stretching shrinking horizontal cylinder. *Results Phys.* **2021**, *21*, 103812. [CrossRef]

22. Abdelmalek, Z.; Qureshi, M.Z.A.; Bilal, S.; Raza, Q.; Sherif, E.S.M. A case study on morphological aspects of distinct magnetized 3D hybrid nanoparticles on fluid flow between two orthogonal rotating disks: An application of thermal energy systems. *Case Stud. Therm. Eng.* **2021**, *23*, 100744. [CrossRef]

23. Muhammad, K.; Hayat, T.; Alsaedi, A.; Ahmad, B. Melting heat transfer in squeezing flow of basefluid (water), nanofluid (CNTs + water) and hybrid nanofluid (CNTs + CuO + water). *J. Therm. Anal. Calorim.* **2021**, *143*, 1157–1174. [CrossRef]

24. Shaw, S.; Samantaray, S.S.; Misra, A.; Nayak, M.K.; Makinde, O.D. Hydromagnetic flow and thermal interpretations of Cross hybrid nanofluid influenced by linear, nonlinear and quadratic thermal radiations for any Prandtl number. *Int. Commun. Heat Mass Transf.* **2022**, *130*, 105816. [CrossRef]

25. Sen, S.S.S.; Das, M.; Mahato, R.; Shaw, S. Entropy analysis on nonlinear radiative MHD flow of diamond-Co_3O_4/ethylene glycol hybrid nanofluid with catalytic effects. *Int. Commun. Heat Mass Transf.* **2021**, *129*, 105704. [CrossRef]

26. Nayak, M.K.; Pandey, V.S.; Shaw, S.; Makinde, O.D.; Ramadan, K.M.; Henda, M.B.; Tlili, I. Thermo-fluidic significance of non Newtonian fluid with hybrid nanostructures. *Case Stud. Therm. Eng.* **2021**, *26*, 101092. [CrossRef]

27. Nayak, M.K.; Shaw, S.; Waqas, H.; Muhammad, T. Numerical computation for entropy generation in Darcy-Forchheimer transport of hybrid nanofluids with Cattaneo-Christov double-diffusion. *Int. J. Numer. Methods Heat Fluid Flow* **2022**, *32*, 1861–1882. [CrossRef]

28. Shaw, S. Impact of cattaneo–Christov heat flux On Al_2O_3–Cu/H_2O–$(CH_2OH)_2$ hybrid nanofluid flow between two stretchable rotating disks. In *Energy Systems and Nanotechnology*; Tripathi, D., Sharma, R.K., Eds.; Advances in Sustainability Science and Technology; Springer: Singapore, 2021. [CrossRef]

29. Mahanthesh, B.; Shehzad, S.A.; Ambreen, T.; Khan, S.U. Significance of Joule heating and viscous heating on heat transport of MoS2–Ag hybrid nanofluid past an isothermal wedge. *J. Therm. Anal.* **2021**, *143*, 1221–1229. [CrossRef]

30. Haq, F.; Khan, M.I.; El-Zahar, E.M.; Khan, S.U.; Farooq, S.; Guedri, K. Theoretical investigation of radiative viscous hybrid nanofluid towards a permeable surface of cylinder. *Chin. J. Phys.* **2022**, *77*, 2761–2772. [CrossRef]

31. Seth, G.S.; Sarkar, S.; Makinde, O.D. Combined free and forced convection couette-hartmann flow in a rotating channel with arbitrary conducting walls and hall effects. *J. Mech.* **2016**, *32*, 613–629. [CrossRef]

32. Seth, G.S.; Sharma, R.; Sarkar, S. Natural convection heat and mass transfer flow with hall current, rotation, radiation and heat absorption past an accelerated moving vertical plate with ramped temperature. *J. Appl. Fluid Mech.* **2015**, *8*, 7–20.

33. Li, P.; Abbasi, A.; El-Zahar, E.R.; Farooq, W.; Hussain, Z.; Khan, S.U.; Khan, M.I.; Farooq, S.; Malik, M.; Wang, F. Hall effects and viscous dissipation applications in peristaltic transport of jeffrey nanofluid due to wave frame. *Colloids Interface Sci. Commun.* **2022**, *47*, 100593. [CrossRef]

34. Hussain, Z.; Al-Khaled, K.; Ashrif, U.; Abbasi, A.; Khan, S.U.; Farooq, W.; Khan, M.I.; Farooq, S.; Malik, M.Y. A mathematical model for radiative peristaltic flow of Jeffrey fluid in curved channel with Joule heating and different walls: Shooting technique analysis. *Ain Shams Eng. J.* **2022**, *13*, 101685. [CrossRef]

35. Javid, K.; Riaz, M.; Chu, Y.M.; Khan, M.I.; Khan, S.U.; Kadry, S. Peristaltic activity for electro-kinetic complex driven cilia transportation through a non-uniform channel. *Comput. Methods Programs Biomed.* **2021**, *200*, 105926. [CrossRef]

36. Abbasi, A.; Mabood, F.; Farooq, W.; Khan, S.U. Radiation and joule heating effects on electroosmosis-modulated peristaltic flow of Prandtl nanofluid via tapered channel. *Int. Commun. Heat Mass Transf.* **2021**, *123*, 105183. [CrossRef]

37. Animasaun, I.L.; Shah, N.A.; Wakif, A.; Mahanthesh, B.; Sivaraj, R.; Koriko, O.K. *Ratio of Momentum Diffusivity to Thermal Diffusivity: Introduction, Meta-Analysis, and Scrutinization*; Chapman and Hall/CRC: New York, NY, USA, 2022; ISBN-13 978-1032108520. [CrossRef]

38. Chu, Y.-M.; Khan, M.I.; Khan, N.B.; Kadry, S.; Khan, S.U.; Tlili, I.; Nayak, M. Significance of activation energy, bio-convection and magnetohydrodynamic in flow of third grade fluid (non-Newtonian) towards stretched surface: A buongiorno model analysis. *Int. Commun. Heat Mass Transf.* **2020**, *118*, 104893. [CrossRef]

39. Song, Y.Q.; Hamid, A.; Sun, T.C.; Khan, M.I.; Qayyum, S.; Kumar, R.N. Chinram unsteady mixed convection flow of magneto-williamson nanofluid due to stretched cylinder with significant non-uniform heat source/sink features. *Alex. Eng. J.* **2022**, *61*, 195–206. [CrossRef]

40. Khan, M.I.; Kadry, S.; Chu, Y.M.; Waqas, M. Modeling and numerical analysis of nanoliquid (titanium oxide, graphene oxide) flow viscous fluid with second order velocity slip and entropy generation. *Chin. J. Chem. Eng.* **2021**, *31*, 17–25. [CrossRef]

41. Khan, M.I.; Nasir, T.; Hayat, T.; Khan, N.B.; Alsaedi, A. Binary chemical reaction with activation energy in rotating flow subject to nonlinear heat flux and heat source/sink. *J. Comput. Des. Eng.* **2020**, *7*, 279–286.

42. Khan, M.W.A.; Hayat, T.; Alsaedi, A. Numerical solution of MHD flow of power law fluid subject to convective boundary conditions and entropy generation. *Comput. Methods Programs Biomed.* **2019**, *188*, 105262. [CrossRef]